PHYSICAL REVIEW E **69**, 021901 (2004)

Absolute interfacial distance measurements by dual-wavelength reflection interference contrast microscopy

Jörg Schilling, Kheya Sengupta,* Stefanie Goennenwein, Andreas R. Bausch,† and Erich Sackmann
E-22 Biophysik, Physik Department, Technische Universität München, James-Franck-Strasse, D-85748 Garching, Germany

(Received 21 May 2003; published 12 February 2004)

Dual-wavelength reflection interference contrast microscopy (DW-RICM) is established as a microinterferometric technique to measure absolute optical distances between transparent planar substrates and hard or soft surfaces such as colloidal beads or artificial and biological membranes, which hover over the substrate. In combination with a fast image processing algorithm the technique was applied to analyze the trajectories of colloidal beads sedimenting under gravity. As the beads approach the surface of the substrate, they slow down because of hydrodynamic coupling of the bead motion to the substrate. The effective surface friction coefficients were measured as a function of the absolute distance of the beads from the surface. The height dependence of the friction coefficient was found to be in quantitative agreement with previous theoretical predictions. Furthermore, we demonstrate that the DW-RICM technique allows the determination of the height of membranes above substrates and the amplitude and direction of height fluctuations. Without any further need to label the membrane the unambiguous reconstruction of the surface profile of soft surfaces is possible.

DOI: 10.1103/PhysRevE.69.021901 PACS number(s): 87.68.+z, 68.47.Pe, 87.64.Rr, 83.85.Jn

I. INTRODUCTION

The technique of reflection interference contrast microscopy (RICM) was originally introduced to observe adhesion of cells and to visualize focal contacts without the need for fluorescent labeling [1]. Quantitative RICM has been applied in the past to measure the local bending elastic modules of red blood cells by spectral analysis of the membrane bending fluctuations [2]. Further, the local adhesion strengths of cells [3] and of giant vesicles [4] could be measured quantitatively by contour analysis of these soft shells close to the substrate. An advantage of the RICM technique over other optical techniques like microellipsometry [5] is that it exhibits high sensitivity below water. In combination with dynamic image processing, rapid measurements of distances with 10 ms time resolution are possible. Over the last few years the technique to study stratified films by RICM has been improved in various ways. A contrast enhancement technique was developed which is based on coating the substrate with a thin film of transparent, low refractive index material such as MgF_2 [6]. The theoretical basis of the technique has been improved by accounting for the divergence of the incident light beam [6] and the nonlocal contributions to the image formation associated with the spatial and temporal variations of the curvature of nonplanar interfaces [7]. More recently a scanning type RICM technique has been developed which allows the study of the dynamics of wetting by partially wetting fluids on solid surfaces [8].

The major drawback of conventional RICM technique is that the information about the absolute phases of the beams reflected by the various interfaces of a stratified film is not known. Therefore, absolute distances cannot be measured. This also implies that it is not possible to determine unambiguously the direction of the local vertical deflections of fluctuating interfaces, for example, those arising from local bending excitations of soft membranes [2]. In this paper we demonstrate that this drawback can be overcome by comparing the interferograms obtained simultaneously with two different wavelengths. In other words, by observing a second wavelength an additional periodicity and boundary condition is introduced. This enables the measurement of absolute distances of colloidal beads above a planar surface with an accuracy of ±3 nm.

In the past, colloidal beads hovering over surfaces have been extensively used as force probes to determine weak interfacial interaction forces of the order of femtonewtons [5,9–13]. The height of the bead was probed by conventional RICM and the interaction potential was reconstructed by measuring the distribution of the mean-square displacements of the beads undergoing Brownian motion. The frictional coefficient characterizing the hydrodynamic interaction of the colloidal probes with the surface was obtained from the time correlation functions of the random displacements. The colloidal probe technique, in conjunction with total internal reflection microscopy has more recently been employed to measure the weak retarded van der Waals interaction [11], to probe the hydrodynamics [12], to determine the charge of colloidal beads [14], and to probe interactions under nonequilibrium conditions [15].

In the recent past there has been a strong interest in the behavior of colloidal particles close to hard surfaces, which is still poorly understood [16,17]. An essential first step in understanding such systems is to reconstruct the three dimensional potential in which the colloidal particles reside. This can be done by following the position fluctuations of the beads by various microscopic methods. However, most of these techniques allow the measurement of either the in-plane or the out-of-plane fluctuations. DW-RICM offers an unique opportunity to simultaneously track both the in-plane

---

*Electronic address: ksengupt@ph.tum.de

†Electronic address: abausch@ph.tum.de

and the out-of-plane fluctuations of the beads.

In the present work the dual-wavelength technique (DW-RICM), in combination with a fast image processing algorithm, is first applied to follow the trajectories of colloidal beads sedimenting under gravity. The sedimentation velocity of the beads was analyzed in terms of the modified Stoke's law of the frictional forces on spherical objects moving close to surfaces [18,19]. Thereby the velocity of the beads is expected to be drastically reduced as they approach the surface. Quantitative agreement with theoretical predictions of [18,19] was obtained. This enables us to measure surface friction coefficients as a function of the absolute bead height of solid surfaces covered by thin films of hyaluronic acid (HA), which is an ubiquitous polysaccharide of the extracellular matrix and can be used to generates a soft surface coverage [20].

We further show that the DW-RICM technique is well suited to measure local distances between lipid bilayer membranes and solid substrates. The fast image processing software [21] enables us to determine both the direction and the absolute height of local deflections of membranes exhibiting thermally excited bending fluctuations. With conventional RICM these information were not accessible.

II. MATERIALS

Substrates. Glass cover slides were cleaned thoroughly by sonicating them in a 2 vol.% detergent solution (Hellmanex *Hellma*, Germany) followed by repeated washing and sonication in pure deionized water (*Millipore*, France). This cleaning procedure renders the glass highly hydrophilic and imparts a high negative charge to it.

Soft polymer films were generated by surface grafting of HA. The molecule exhibits one negative charge per repeat unit and the procedure for HA deposition has been described elsewhere [20]. In brief, the cleaned glass slides were coated (by Langmuir-Blodgett/Langmuir-Schaefer technique) with a lipid bilayer bearing metal-chelating groups. A naturally occurring HA-binding protein called p32 was genetically modified to exhibit a histidine tag which can bind to metal-chelating groups. This modified p32 was bound to the deposited lipid bilayer and finally HA was bound to the p32, both by simply incubating the ingredients together.

Beads. Polystyrene beads were obtained from *Polysciences Industries*, Washington, PA with a diameter of 10.5 ± 1.3 μm. The beads were used either after washing in millipore water (referred to as bare beads) or after coating with Bovine Serum albumin (BSA) (purchased from *Sigma-Aldrich*, Germany) followed by a washing step (referred to as BSA-beads).

Vesicles. Giant vesicles were prepared following the electroswelling method of Ref. [22]. Lipids were dissolved in chloroform (1 mg ml^{-1}). Some droplets ($\simeq$10–50 μl) were deposited onto indium-tin-oxide (ITO) electrodes and stored in a vacuum chamber for at least 12 h so that the solvent was evaporated completely. The swelling chamber consisted of two teflon wells, pressed together by screws. The chamber was filled with 2 ml of a 170 mM sucrose solution and the ITO electrodes were opposed to each other as in a capacitor. Then an ac electric current of 10 Hz and 1 V was applied for 2 h while the whole chamber was kept at 40 °C. Under these conditions giant vesicles formed spontaneously by a self-assembly process.

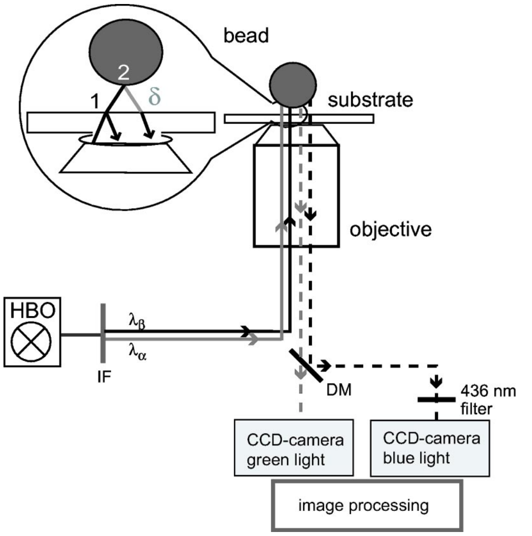

FIG. 1. Schematic view of the dual-wavelength RICM setup consisting of an *Axiomat* (Zeiss, Germany) inverted microscope equipped with an antiflex, 63×, oil immersion, N.A.=1.3, Zeiss, objective. The sample is illuminated through the objective by two monochromatic light beams ($\lambda_\alpha = 546$ nm, $\lambda_\beta = 436$ nm) generated by passing the light from a 100-W mercury vapor lamp (*Osram*, Germany) through a interference filter (IF) that allows the two selected wavelengths (green and blue) to pass through. The beams reflected from the sample are separated by a dichroic mirror (DM) and a filter (436 nm). They are projected onto two separate charged-coupled device cameras (10 bit camera Hamamatsu, Japan) with two different image processing units. The image recording is done at approx. 100 Hz and the analysis of the height can be performed immediately from the stored data. Inset at upper left: Representation of the image formation by interference of light reflected from the top surface of the substrate (interface 1) and the bottom substrate of the object (interface 2).

Buffers. All the experiments were done in 5 mM or 20 mM HEPES buffer as specified. The ionic strength was adjusted by adding KCl.

III. RICM TECHNIQUE

Conventional RICM. As illustrated in the inset of Fig. 1, the RICM images are formed by superposition of the light waves reflected from the top surface of the underlying planar substrate (intensity I_1) and from the bottom surface of the object under observation (intensity I_2). The intensities I_1 and I_2 are related to the intensity of the incident beam by Fresnel's law. The contributions of the stray light to the image is suppressed by the antiflex illumination technique [23]. The incident linearly polarized light is rendered circularly polarized by a quarter-wave plate integrated with the objective. Reflection at both interfaces of the sample (1,2) reverses the direction of polarization of this circularly polarized light. When it passes through the quarter-wave plate again, it emerges as linearly polarized light but with the polarization turned by an angle of $\pi/2$ with respect to the incident light. A second polarizer, crossed by $\pi/2$ with respect to the first one, allows this light to go through but cuts off all stray light reflected from other surfaces.

The intensity distribution of the interference pattern for a given wavelength is given by

$$I(h(x,y),\lambda)=I_1+I_2+2\sqrt{I_1I_2}\,\cos\left(\frac{4\pi nh(x,y)}{\lambda}+\delta\right), \tag{1}$$

where $I(h(x,y),\lambda)$ is the intensity on the interferogram corresponding to a point whose lateral position is defined by the coordinates (x,y) and the height is given by $h(x,y)$. n is the refractive index of the medium and δ is the phase shift of the light reflected from the object. The intensities I_1 and I_2 are unknown. For images exhibiting Newton fringes they can, however, be expressed in terms of the minimum (I_{min}) and maximum (I_{max}) intensities of the interference pattern. The curvature of the object has been neglected here and only incident and reflected light rays that are parallel to the optical axis have been considered. The corrections due to the curvature of the object can be accounted for by applying the nonlocal theory [7]. The following relation between the height $h(x,y)$ and the intensity distribution $I(h(x,y),\lambda)$ of the RICM image is obtained [6].

$$\frac{2I(h(x,y),\lambda)-(I_{max}+I_{min})}{I_{max}-I_{min}}=\cos\left(\frac{4\pi nh(x,y)}{\lambda}+\frac{p\lambda}{2\pi}\right),$$

where p is an integer and $p\lambda/2\pi$ accounts for the unknown phase of the reflected beams. Inverting Eq. (2) yields the height but with an ambiguity of a factor of $\Delta h=p\lambda/2\pi$. Equation (2) assumes a point light source. For a finite aperture, the term $\sqrt{I_1I_2}$ in Eq. (1) has to be replaced by $\gamma_{12}\sqrt{I_1I_2}$, where $\gamma_{12}=\sin\{2qh(x,y)\sin^2\alpha/2\}/2qh(x,y)\sin^2\alpha/2$ (α is the aperture angle and q is the wave number given by $q=2\pi/\lambda$). The factor γ_{12} results in a decrease of the difference $I_{max}-I_{min}$. Moreover, the phase $4\pi h(x,y)/n$ is stretched by a factor $\sqrt{1-\sin^2\alpha/2}$.

DW-RICM technique. The intensity $I(h(x,y),\lambda)$ in Eq. (2) can be considered as a parametric representation of a periodic function with h as the variable parameter. In the case where information about the intensity is available for two wavelengths (say, λ_α and λ_β), the phase $p\lambda/2\pi$ can be eliminated from Eq. (2) and I_β can be expressed as a function of I_α (where I_α and I_β are the corresponding intensities).

$$I_\beta=D_\alpha-S_\beta\cos\left(\frac{\lambda_\alpha}{\lambda_\beta}\right)\cos^{-1}\left(\frac{D_\beta-I_\alpha}{S_\alpha}\right), \tag{2}$$

where $D_\alpha=I_\alpha^{max}-I_\alpha^{min}$, $S_\alpha=I_\alpha^{max}+I_\alpha^{min}$, and $S_\beta=I_\beta^{max}+I_\beta^{min}$. It is most instructive to display I_α and I_β in a parametric plot with h as parameter as shown in Fig. 2. From this figure it becomes clear that to every pair of values I_α and I_β an unambiguous height h can be assigned that fulfils Eq. (2).

A different approach yielding a better insight into the range of unambiguity of the present technique can be gained by considering plots of the normalized intensities $\tilde{I}_\alpha$ and $\tilde{I}_\beta$ as a function of the height $h(x)$ (see Fig. 3). Here the periodicity of the intensity of each wavelength is shown, alternating between a minimum (0) and maximum (1) value, which corresponds to destructive and constructive interference, respectively. The two oscillating functions I_α (546 nm) and I_β (436 nm) exhibit a common periodicity of 816 nm (cf. Fig. 3), which defines the upper limit of the unambiguity of the technique with this choice of λ_α and λ_β.

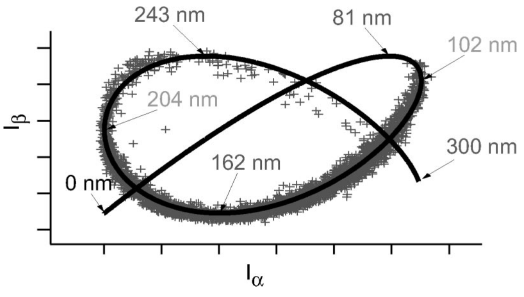

FIG. 2. Plot of the intensity I_α corresponding to wavelength λ_α against the intensity I_β corresponding to wavelength λ_β. The solid line is plotted according to Eq. (2). The crosses represent the corresponding experimental data from a fluctuating bead. The data were collected by following the Brownian motion of a bead hovering above a substrate of hyaluronic acid fluctuating between a height of about 100 and 270 nm. The images from the two different wavelengths were recorded with two different cameras as shown in Fig. 1. The beads were tracked by the algorithm explained later and the intensities of their centers were monitored.

Dynamic determination of the in-plane position of beads. The interferogram of a bead depends sensitively on its height over the substrate. Since the beads exhibit three-dimensional Brownian motion, i.e., they fluctuate both out-of-plane (vertical) and in-plane (horizontal) around a mean position. The out-of-plane movement leads to drastic changes in the interferogram with time. The center of the bead appears dark at one moment and bright some instances later, additionally the diameter of the interference rings increase or decrease, depending whether the bead moves up or down in the observed

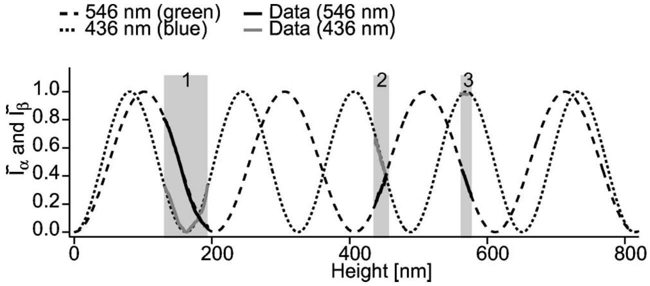

FIG. 3. Normalized Intensities $\tilde{I}_\alpha$ and $\tilde{I}_\beta$ plotted as a function of the height, according to Eq. (2). The dotted lines represent the theoretical curves Eq. (2) and the heavy stretches (indicated by 1, 2, and 3) represent data for three different beads fluctuating above different substrates (polymer films of different thicknesses on glass substrates). The heights are calculated according to Eq. (4). For the data shown here, the beads fluctuate in time from 140 to 200 nm for position 1, from 420 to 460 nm for position 2, and from 540 to 590 nm for position 3.

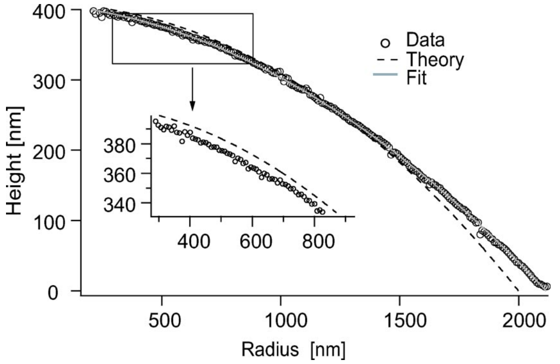

FIG. 4. Plot of the height calculated according to Eq. (2) against the radius of the corresponding circular fringe measured from the interferogram. The crosses are the data and the dotted line represents the theoretical expectation according to Eq. (3). The drawn line is a polynomial fit to the data, given by Eq. (4).

time interval. The in-plane motion leads to a lateral shift of the interferogram, which requires the tracking of the beads position in lateral direction. Due to the complicated changes in the interferogram as the bead fluctuates, it is not possible to track the bead by conventional tracking techniques such as convolution with a mask. Therefore a new tracking algorithm is needed which is independent of the details of the intensity distribution in the image. To achieve this, an algorithm which exploits the spherical symmetry of these beads was developed. It allows a subpixel determination of the lateral position and is described in the Appendix.

Determination of the out-of-plane position of beads. As explained before, in the conventional RICM technique, the height $h(x,y)$ is determined by measuring the intensity $I(h(x,y),\lambda)$ at that point. Since it is difficult to measure and compare absolute intensities, we have developed a technique to measure the height of the beads which makes use of the circular symmetry of the interferogram arising from the spherical symmetry of the beads. The interferogram of a bead hovering over a planar substrate consists of a concentric array of circular interference fringes. From simple geometrical optic considerations, the height h is related to the radius r_l of the lth interference ring according to

$$h(r_l)=\frac{\lambda l}{2n}-R+\sqrt{R^2-r_l^2}, \tag{3}$$

where R is the radius of the bead. To get an idea of the error involved in assuming such a simple relation, we plot in Fig. 4 the bead height [calculated from the measured intensity values according to Eq. (2)] against the experimentally determined radius of the corresponding interference ring. The agreement between the data and the theoretical curve according to Eq. (3) is fairly good for radii r_l smaller than 1500 nm. Above $r_l=1500$ nm, the corrections arising from the finite curvature of the bead get important and Eq. (2) is no longer applicable. This error could be overcome by applying the nonlocal theory [7]. A smaller but still significant discrepancy is observed for small values of the ring radius where the height, as determined from intensity considerations [Eq. (2)], is lower than the height expected from geometrical considerations [Eq. (3)], which is due to the fact that the pixel resolution is below the optical resolution. In order to account for these corrections, we fitted the data to the following polynomial law:

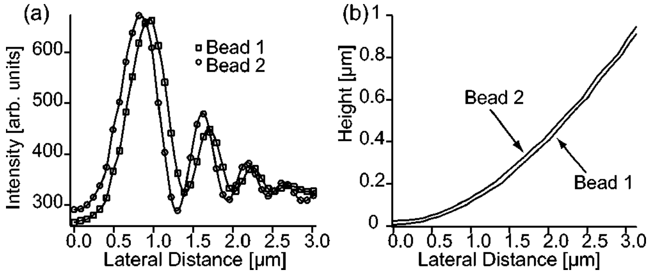

FIG. 5. (a) Intensity distribution (averaged over the full 2π angle) along the radial direction for two different beads at heights of 4 nm and 29 nm. The drawn curves define the optimal fits of Eq. (2) to the data points which are indicated by open circles and open squares for the two different beads. (b) Reconstructed profile according to Eq. (4) of the two beads shown in (a).

$$f(r)=408.7-0.027\,04r-0.000\,078\,6r^2, \tag{4}$$

shown in Fig. 4. This empirical equation was used to determine the height of the beads in the present work. Note, that Eq. (4) holds only for beads of diameter of 10.5 μm. For beads of other diameter the coefficients would be different.

To demonstrate the accuracy of the height measurements, we present in Fig. 5 the intensity distribution of the interferograms of two beads whose bottom-most points are at heights of 4 nm and 29 nm, respectively, above the surface of the substrate. Care was taken to choose beads of equal diameter (as determined from independent bright-field measurements). Though typically latex beads may have protrusions of several nanometers, such large protrusions disfigure the circular pattern of the RICM interferograms. Care was taken to choose beads whose interferograms were not marred by the presence of protrusions. Further, the effect of small unevenness of the surfaces of the beads was minimized by taking radial averages. The height profiles were reconstructed and are shown in Fig. 5. The expected profile representing a part of the cross section of the spherically symmetric beads is recovered (it should be noted that the expected profile is not strictly circular since the corrections due to the curvature of the bead has not been taken into account). The fact that at each point along the reconstructed profile the heights of the beads differ by 25±6 nm, indicates that the profiles can be reconstructed with 6-nm accuracy.

The error introduced in the height measurement due to errors in measuring the radius is given by

$$\Delta h(r_i)=\sqrt{\left[\left(\frac{R}{R^2-r_i^2}\right)\Delta R\right]^2+\left(\frac{r_i\Delta r_i}{\sqrt{R^2-r_i^2}}\right)^2}, \tag{5}$$

where ΔR and Δr_i are the errors in measuring the bead radius, and the ring radius, respectively. As an example, for a bead of radius 10 μm at a height of 100 nm, an error of 100 nm in the bead radius and an error of 10 nm in the ring radius gives rise to an error of 6 nm in the height.

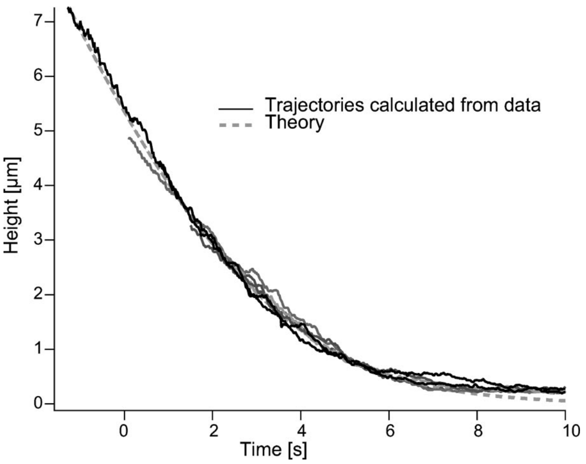

FIG. 6. Height versus time plot of five different beads sedimenting under gravity. The thin noisy lines are experimentally determined trajectories for bare beads falling in HEPES buffer above a bare glass substrate. The noise in the data is due to thermal fluctuations of the beads. The thick dotted line is a fit to Eq. (7) with the density difference between the bead and the medium $\Delta\rho = 53\ \mathrm{kg\,m^{-3}}$.

IV. RESULTS

A. Sedimentation of beads under gravity

The trajectories of beads sedimenting under gravity can be reconstructed in real time using our fast image processing technique. Due to the divergence of the incident light rays, RICM interferograms are clearly visible only for bead heights up to about 7 μm with our setup. In Fig. 6 examples of experimentally observed trajectories of beads sedimenting under gravity are shown as thin unsteady lines.

The expected height z of the bead at a time t is determined by the equilibrium between the gravitational force and viscous force

$$6\pi\eta_{eff}(z)R\frac{dz}{dt}=\frac{4}{3}\pi R^3\Delta\rho g, \tag{6}$$

where $\Delta\rho$ is the density difference between the bead and the medium, g is the acceleration due to gravity, R is the bead radius, $\eta_{eff}(h)$ is the effective height dependent viscosity, dz is an infinitesimal increment in the distance through which the bead falls and dt is the time it takes to fall through distance dz.

Integration of Eq. (6) yields

$$\int_{z=h_o}^{h}\eta_{eff}(z)dz=-\frac{2\Delta\rho R^2 g}{9}(t-t_0), \tag{7}$$

where h_o is the initial height and t_o is the corresponding time.

For a spherical bead moving close to a rigid wall the friction coefficient $\gamma(h)$ is determined by the coupling of the hydrodynamic flow field of the bead with the substrate and can be expressed in terms of the modified Stoke's law [9,18]: $\gamma(h)=6\pi\eta R\Lambda(h/R)$ where η is the bulk viscosity of the solvent, and $\Lambda(h/R)$ is the correction factor to account for the hydrodynamic coupling between the bead and the wall [18,19] and therefore $\eta_{eff}(h)=\eta\Lambda(h/R)$ is the effective viscosity. For the out-of-plane motion, $\Lambda(h/R)$ is given by

$$\Lambda(h/R)=\frac{4}{3}\ \sinh(h/R)\ \Sigma_n\frac{n(n+1)}{(2n-1)(2n+3)}\left(\frac{2\sinh[(2n+1)(h/R)]+(2n+1)\sinh(2h/R)}{4\sinh[(2n+1)(h/R)]-(2n+1)2\sinh(2h/R)}-1\right). \tag{8}$$

For small h/R this reduces to $\Lambda(h/R)=R/h$, such that

$$\eta_{eff}=\eta_{bulk}R/h. \tag{9}$$

The thick dotted line in Fig. 6 is a fit to Eq. (7) with the value of η_{eff} from Eq. (8). It can be seen that the experimental trajectories closely follow the calculated trajectory.

Steady state dynamics of fluctuating beads. With the DW-RICM technique, it is possible to simultaneously measure the height and the effective viscosity felt by fluctuating beads. This provides an unique opportunity to test the validity of Eq. (8). The effective viscosity can be determined by fitting the height correlation function $\langle h(t)h(t+\tau)\rangle$ to an exponential function given by

$$\langle h(t)h(t+\tau)\rangle=\frac{k_BT}{V''}\exp\left(-\frac{V''\tau}{\gamma_{eff}(h)}\right), \tag{10}$$

where V'' is the spatial double derivative of an effective interfacial potential and $\gamma_{eff}(h)$ is an effective friction coefficient (see Refs. [9,10], or [20] for more detailed description). As discussed above, $\gamma(h)=6\pi\eta_{eff}(h)=6\pi\eta\Lambda(h/R)$, where $\Lambda(h/R)$ is given by Eq. (8). In Fig. 7 we have plotted the observed $\eta_{eff}(h)$ as a function of the height h for beads hovering over a soft polyelectrolyte film made of HA. The bead height was controlled by addition of a monovalent salt. The solid lines are generated by taking $\Lambda(h/R)$ from Eq. (8) for η=1, 1.5 and 2 mPa s. It can be seen that the effective viscosity experienced by the beads correspond to values of the bulk viscosity between 1 and 2 mPa s. The height dependence of the viscosity clearly follows the theoretical prediction.

B. Determination of membrane fluctuations

The development of the DW-RICM technique was stimulated by previous studies of the physics of cell adhesion at

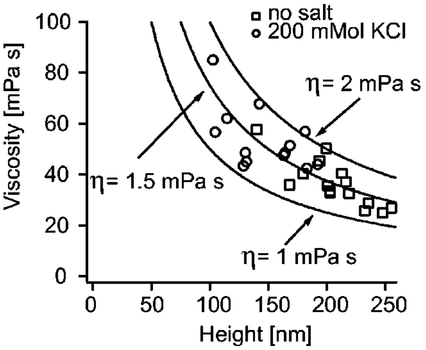

FIG. 7. The observed viscosity $\eta_{eff}(h)$ plotted against the height for beads fluctuating near a surface. The symbols represent different beads hovering over a soft polymer film of hyaluronic acid. Note that the variability for each symbol is due to the heterogeneity of HA films. The solid lines are generated from Eq. (8) for η=1, 1.5, and 2 mPa s.

our laboratory whereby a method for the measurements of the adhesion strengths of soft elastic shells (giant vesicles or cells) was developed [4]. This technique is based on the analysis of the contour and shape changes of the soft shells hovering over planar surfaces by RICM. A further problem arises when the adhering membranes exhibit pronounced (thermally excited) bending fluctuations which give rise to a generic (entropy driven) repulsion force and thus contribute to the interfacial interaction potential [24]. In order to determine interaction potentials as a function of the membrane-substrate distances it is necessary to measure both the absolute height of the soft surface and the direction of local deflections of undulating membranes which is not possible with the conventional RICM. Below we show that DW-RICM can overcome these drawbacks [26].

The leopardlike intensity pattern of the contact area of a giant vesicle with a planar glass substrate is shown in Fig. 9(a). It represents the instantaneous deflection of the soft membrane. From a single wavelength micrograph it is not possible to determine the absolute value of the local membrane deflection or the direction of the deflection due to the arbitrary phase of the reflected light.

The DW-RICM technique allows us to determine the absolute height of a fluctuating small area of the vesicle membrane in time.

As in the example of the position analysis of colloidal beads we can determine the absolute height of a point (x,y) within the contact area of the membrane by a parametric plot of the intensities as a function of the height h. Again the reflected intensity of the green wavelength I_α is plotted against the reflected intensity of the blue wavelength I_β. A comparison of the obtained data to the numerical curve [black line in Fig. 8(b)] reveals that the membrane fluctuates in time between 0 and 120 nm above the substrate. The large scatter of the data at a given height (approx 30%) is attributed to bending fluctuations of the membrane. Further the low reflectivity of membranes compared to PS beads and local lateral phase separations within the membrane increase the noise in the signal.

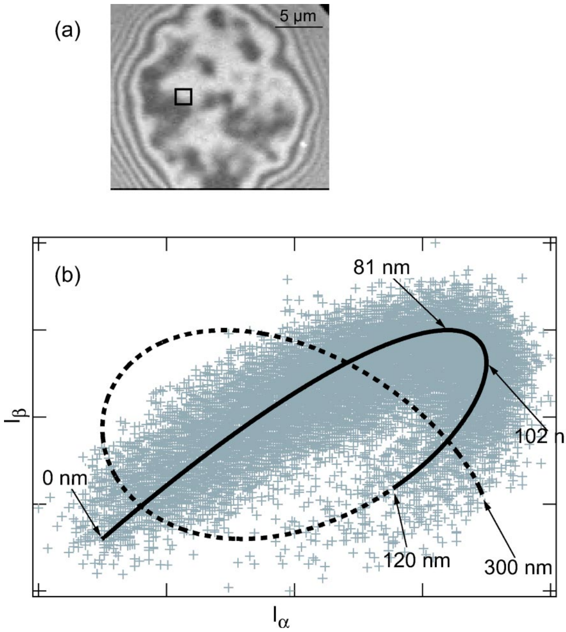

FIG. 8. (a) RICM micrograph of a giant lipid vesicle in contact with a glass substrate. The leopardlike texture displays regions of different heights in the contact area, whereas the interference rings indicate the bending away of the membrane from the substrate. The black square marks a region from where the intensity values are analyzed. (b) The crosses display the measured intensity of the β wavelength I_β versus the intensity of the α wavelength I_α for a 0.6 μm×0.6 μm^2 patch indicated in (a). The line is the parametric plot, according to Eq. (2). The comparison with the experimental data yields that the membrane of the vesicle is fluctuating in time between 0 and 120 nm above the substrate.

Next we discuss the method adopted to determine the direction of one exemplary bending excitation along the line indicated by the arrow in Figs. 9(a) and 9(b). Figure 9(a) is the interferogram of the green wavelength λ_α and Fig. 9(b) shows the micrograph recorded for the blue wavelength λ_β. The height reconstruction along the *x* axis is analyzed by first plotting the intensities of the two wavelength along that line in Fig. 9(d). Although it is possible to conclude that the contact area fluctuates between 0 and 140 nm from the above analysis, the direction of the deflection of the membrane is still ambiguous. The dip in the intensity of λ_α [between the positions 1.5 and 2.5 μm in Fig. 9(d)] can result either from an upward (+) or downward (−) deflection of the membrane, as depicted in Fig. 9c. These two possible reconstructions are also indicated in the height reconstruction from I_α, Fig. 9(e). From this reconstructed height the intensity of λ_β is calculated for each point along the axis according to Eq. (2) and the result is shown in Fig. 9(f). By comparing the calculated intensities with the measured intensity values for λ_β displayed in Fig. 9(d), it is evident that the solid line in Fig. 9c is the correct reconstruction. The deflection is thus directed upward, as indicated by the (+) possibility in the sketch Fig. 9(c).

It should be noted that it is important to evaluate exactly the same position of the membrane on the two cameras. To achieve this the following procedure was developed. A small

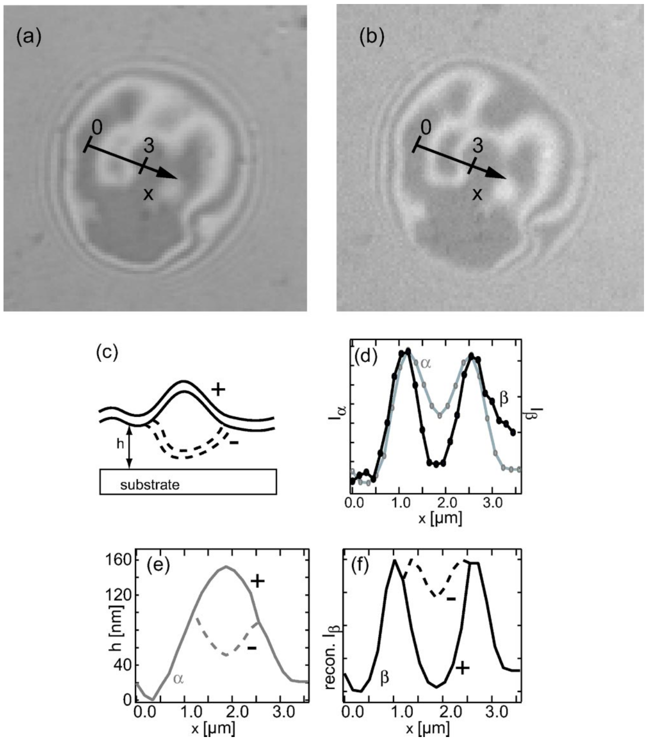

FIG. 9. RICM micrograph of a giant vesicle in contact with a glass substrate. (a) Intensity I_α of the green wavelength and (b) of the blue wavelength I_β along the black x axis are shown. (c) Two possible reconstructions of the membrane profile are depicted schematically and labelled by (+) for the upward deflection and by (−) for the downward deflection. In (d) the intensity of the green (I_α) and blue (I_β) wavelength along this axis is displayed. (e) Two possible surface profiles, denoted by (+) and (−) of the membrane reconstructed from the interferogram I_α are given. They are calculated according to Eq. (2). In (c) the two possible reconstructions are depicted schematically and labeled by (+) for the upward deflection and by (−) for the downward deflection of the membrane. (f) Intensity distribution of the beta wavelength calculated from the two height profiles given in (e). Since the line denoted by (+) agrees with the measured intensity profile displayed in (d), the upward deflection is the correct height reconstruction.

area A_g of the interferogram obtained with the green wavelength is considered. In order to find exactly the same area in the image obtained by the blue wavelength, an approximate position of the area $\widetilde{A}_b$ is first located. Subsequently, the intensity changes in time of area $\widetilde{A}_b$ is correlated with the intensity changes in A_g. By comparing the correlation of different patches around $\widetilde{A}_b$, the position corresponding exactly to A_g is determined by the maximum of these correlation functions, since the intensity changes due to the fluctuation of the membrane motion is almost identical for identical points. Further, a time correlation of A_g and A_b allows the determination of the exact time difference between the two time series recorded.

V. DISCUSSION

In this paper we have demonstrated that dual-wavelength microinterferometry opens up the possibility of measuring absolute values of optical distances between a transparent surface and a reflecting object, which can be nontransparent or transparent (for example a colloidal bead or a lipid membrane). Since the refractive index of the medium is generally known, absolute distances can be determined. In case of spherical beads of known size, the accuracy of the absolute distance measurement is about 6 nm and that of the relative height measurement is 0.5 nm. The accuracy of the relative height measurement can be estimated by looking at the autocorrelation of the data; for bead fluctuations above the limit of resolution, the autocorrelation function ceases to be close to an exponential function and is instead a flat featureless line. To measure the height of objects that are higher than 816 nm, a third wavelength (for example, the 677 nm red line of mercury) can be used [21]. In this case, the simultaneous recording of all the three wavelengths is not necessary. After determining the height using two wavelengths as described above, which yields the height modulo 820 nm, it is enough to reconstruct the relative height from the third wavelength. A comparison with Fig. 3 removes the 820 nm ambiguity. It is advisable to use the third wavelength in conjunction with one of the colors already used before to ensure that the bead did not change its height drastically between the successive experiments.

A fast image processing algorithm was developed which enables measurements of distances of moving beads with 10-ms resolution. This opens up new possibilities of studying simultaneously the hydrodynamic and the static interactions of colloidal beads with solid surfaces. The quantitative agreement of measured effective coefficient of friction between beads and substrates with theoretical considerations by Happel and Brenner [18], demonstrate the power of the technique. Moreover a large macroscopic area can be scanned, which can yield information about the heterogeneities (both in surface profile and in the viscoelastic parameters) of the substrate. This would be specially relevant while probing surface grafted polymer films and the effect of cross linkers on such a system [20]. Since relative height resolution is 0.5 nm this method is limited to the measurement of potential strengths (characterized in terms of the double derivation of the potential) of about $10k_BT$ nm^{-2}. In combination with magnetic tweezers rheometry, the viscoelastic moduli of stiffer polymer films ought to be accessible.

Unambiguous height reconstruction becomes possible for membranes of vesicles or cell. It is not only possible to determine the absolute height of an adhesion patch but also possible to reconstruct unambiguously the local deformation of the adhering membrane.

ACKNOWLEDGMENTS

The work was supported by the Deutsche Forschungsgemeinschaft (Grant Nos. SFB 563 C5 and B14) and the Fonds der Chemischen Industrie. One of the authors (K.S.) is grateful for the financial support by the Humboldt Foundation.

APPENDIX

Determination of the temporary lateral position of colloidal beads

In the following we describe a procedure for determining the position of the center of symmetry of RICM interferograms of spherical beads without application of the refined (finite aperture and nonlocal image formation) theories of RICM image formation. By making use of the well known optical transfer function of spherical objects the bead position is determined by searching for the global center of symmetry of the interference pattern by the following algorithm.

First, an arbitrary point $\vec{x}$ is chosen near the real center of the interferogram of the bead. Next, the average intensities $\langle I_i(\vec{x})\rangle$ along circles of increasing radii centered around $\vec{x}$ are calculated according to

$$\langle I(\vec{x},r_i)\rangle = \frac{1}{2\pi}\int_{\phi=0}^{2\pi} I(\vec{x}+\vec{r}_{i,\phi})\,d\phi, \tag{A1}$$

with $i=1\ldots N$, where r_i is the radius of the ith circle and the distance $(r_i - r_{i-1})$ between two circles is equal to the pixel size. $\phi=0\ldots 2\pi$ is the angle that is averaged over to get the average intensity for each circle. The number of circles considered is typically $N\approx 37$.

If $\vec{x}$ coincides with the real center of symmetry of the pattern, the intensity $I(\vec{x}+\vec{r}_{i,\phi})$ at each of the points $\vec{x}+\vec{r}_{i,\phi}, \phi=0\ldots 2\pi$ along a circle i will be equal to (or be very close in value to) the average intensity $\langle I_i(\vec{x},r_i)\rangle$. A quantity $\sigma^2(I(\vec{x},r_i))$ is now defined for each circle i which is a measure of how different $I(\vec{x}+\vec{r}_{i,\phi})$ at each point $(\vec{x}+\vec{r}_{i,\phi})$ is from $\langle I_i(\vec{x},r_i)\rangle$.

$$\sigma^2(I(\vec{x},r_i)) = \frac{1}{2\pi}\int_{\phi=0}^{2\pi}[I(\vec{x}+\vec{r}_{i,\phi}) - \langle I(\vec{x},r_i)\rangle]^2 d\phi. \tag{A2}$$

$\sigma(I(\vec{x},r_i))$ is a measure of the proximity of the arbitrarily chosen point $\vec{x}$ to the real center of symmetry. If $\vec{x}$ is close to the center, $\sigma(I(\vec{x},r_i))$ is small for each circle i whereas, if $\vec{x}$ is far from the real center, $\sigma(I(\vec{x},r_i))$ is large for each circle.

Next, a quantity σ_{tot} is defined as $\sigma_{tot}(\vec{x}) = \Sigma_{i=1}^{N}\sigma(I(\vec{x},r_i))$. The global center of the intensity distribution should be at the point where $1/\sigma_{tot}(\vec{x})$ is maximum. In other words, in principle, the center can be identified by maximizing $1/\sigma_{tot}(\vec{x})$ with respect to the position vector $\vec{x}$.

But there is an additional effect that has to be taken into consideration. A point that lies in the featureless background of the image (or a part of the image where the intensity varies monotonously) will also give a maximum for $1/\sigma_{tot}(\vec{x})$. To overcome this problem, the gradient in the intensity distribution along the radial direction of the RICM interferogram is considered. The radial gradient in the intensity is low in the featureless background whereas it is the highest when $\vec{x}$ coincides with the center of symmetry of the interferogram.

Consider the difference in the average intensity between two consecutive circles

$$D_i(\vec{x}) = \langle I(\vec{x},r_i)\rangle - \langle I(\vec{x},r_{i+1})\rangle. \tag{A3}$$

This quantity is large for each i if the origin of the circle chosen coincides with the real center of symmetry of the interferogram. $D_i(\vec{x})$ is now averaged over all the circles to get $\langle D(\vec{x})\rangle = (1/N)\Sigma_i^N D_i(\vec{x})$. Note that $\langle D(\vec{x})\rangle$ is also large if $\vec{x}$ lies at a point where the intensity shows a monotonous gradient away from the center and not a pattern of maxima and minima that is characteristic of an RICM pattern. To eliminate this possibility, the deviation of $D_i(\vec{x})$ from $\langle D(\vec{x})\rangle$ is calculated: $\sigma_{grad}^2(\vec{x}) = (1/N)\Sigma_i^N[D_i(\vec{x}) - \langle D(\vec{x})\rangle]^2$. Again, this quantity is small when $\vec{x}$ lies in the featureless background and large when $\vec{x}$ coincides with the global center of symmetry. Thus the global center of symmetry can be identified by simultaneously maximizing $1/\sigma_{tot}(\vec{x})$ and $\sigma_{grad}(\vec{x})$, in other words, by maximizing $F(\vec{x}) = \sigma_{grad}/\sigma_{tot}$ with respect to $\vec{x}$.

The next task is to find the radius of the circular fringes. This is done by taking radial intensity averages around the center of symmetry and simply looking for the extremal values. If the procedure described above is performed with pixel resolution the accuracy of the determination of the bead position would be about 20 to 30 nm (for bead heights between 0 and 400 nm). In order to achieve a subpixel accuracy, the following procedure is applied. The intensity distribution is expanded in a Taylor series about the position of the discrete extremum: $I(x) = I(a) + (x-a)I'(a) + \frac{1}{2}(x-a)^2 I''(a)$, where $I'(a)$ and $I''(a)$ are the first and second derivative of the intensity at position a. The extremal values of $I(x)$ are found by the condition $dI(x)/dx = 0$, which yields for the optimal position $x = a - [I'(a)/I''(a)]$.

---

[1] A.S.G. Curtis, J. Cell Biol. **20**, 199 (1964).
[2] A. Zilker, M. Ziegler, and E. Sackmann, Phys. Rev. A **46**, 7998 (1992).
[3] R. Simson, A. Albersdoerfer, and E. Sackmann, Mater. Res. Soc. Symp. Proc. **463**, 3 (1997).
[4] R. Bruinsma, A. Behrisch, and E. Sackmann, Phys. Rev. E **61**, 4253 (2000).
[5] K.R. Neumaier, G. Elender, E. Sackmann, and R. Merkel, Europhys. Lett. **49**, 14 (2000).
[6] J.O. Rädler and E. Sackmann, J. Phys. II **3**, 727 (1993).
[7] G. Wiegand, K.R. Neumaier, and E. Sackmann, Appl. Opt. **37**, 6892 (1998).
[8] B. Ovryn and J.H. Andrews, Appl. Opt. **38**, 1959 (1999).
[9] J.O. Rädler and E. Sackmann, Langmuir **8**, 848 (1992).
[10] M. Kühner and E. Sackmann, Langmuir **12**, 4866 (1996).
[11] D.C. Prieve and N.A. Frej, Langmuir **6**, 396 (1990).
[12] M.A. Bevan and D.C. Prieve, J. Chem. Phys. **113**, 1228 (2000).
[13] M. Gelbert, M. Biesalski, J. Rhe, and D. Johannsmann, Langmuir **16**, 5774 (2000).
[14] H.H. von Gürnberg, L. Helden, P. Leiderer, and C. Bechinger, J. Chem. Phys. **114**, 10 094 (2001).
[15] S.H. Behrens, J. Pelwa, and D.G. Grier, Eur. Phys. J. E **10**, 115 (2003).
[16] J.C. Crocker and D.G. Grier, Phys. Rev. Lett. **77**, 1897 (1996).
[17] R.V. Durand and C. Franck, Phys. Rev. E **61**, 6922 (2000).
[18] J. Happel and H. Brenner, *Low Reynolds Number Hydrodynamics* (Kluwer Academic, London, 1983).

[19] H. Brenner, Chem. Eng. Sci. **16**, 242 (1961).

[20] K. Sengupta, J. Schilling, S. Marx, M. Fischer, A. Bacher, and E. Sackmann, Langmuir **19**, 1775 (2003).

[21] Jörg Schilling, Ph.D. thesis, Universität München, 2003.

[22] D.S. Dimitrov and M.I. Angelova, Bioelectrochem. Bioenerg. **19**, 323 (1988).

[23] J. S. Ploem, *Mononuclear Phagocytes in Immunity, Infection and Pathology* (Blackwell Scientific, Oxford, 1975).

[24] S. Marx, J. Schilling, E. Sackmann, and R. Bruinsma, Phys. Rev. Lett. **88**, 138102 (2002).

[25] P. Fromherz, V. Kiessling, K. Kottig, and G. Zeck, Appl. Phys. A: Solids Surf. **69**, 571 (1996).

[26] A method to measure the absolute distances of membranes from surfaces in the subnanometer range is fluorescence interference contrast microscopy (Ref. [25]). However, this technique requires fluorescent labeling of the membranes as well as the deposition of the membrane on substrates exhibiting 4–16 well defined heights and refractive indices.